Acta Biomaterialia 6 (2010) 1772–1782

Contents lists available at ScienceDirect

Acta Biomaterialia

journal homepage: www.elsevier.com/locate/actabiomat

Corrosion inhibition of powder metallurgy Mg by fluoride treatments ☆

M.D. Pereda [a,b], C. Alonso [c], L. Burgos-Asperilla [c], J.A. del Valle [d], O.A. Ruano [d], P. Perez [d], M.A. Fernández Lorenzo de Mele [a,b,*]

[a] Instituto de Investigaciones Fisicoquímicas Teóricas y Aplicadas (INIFTA, CCT La Plata-CONICET), Facultad de Ciencias Exactas, Universidad Nacional de La Plata, Casilla de Correo 16, Sucursal 4, 1900 La Plata, Argentina
[b] Facultad de Ingeniería, Universidad Nacional de La Plata, Calle 1 y 47, 1900 La Plata, Argentina
[c] Departamento de Química Física Aplicada, Universidad Autónoma de Madrid, 28049 Madrid, Spain
[d] Departamento de Metalurgia Física, Centro Nacional de Investigación Metalúrgica (CENIM), Consejo Superior de Investigaciones Científicas (CSIC), 28040 Madrid, Spain

ARTICLE INFO

Article history:
Received 31 March 2009
Received in revised form 30 September 2009
Accepted 6 November 2009
Available online 11 November 2009

Keywords:
Magnesium
Degradable implant
Magnesium fluoride
Powder metallurgy
SECM

ABSTRACT

Pure Mg has been proposed as a potential degradable biomaterial to avoid both the disadvantages of non-degradable internal fixation implants and the use of alloying elements that may be toxic. However, it shows excessively high corrosion rate and insufficient yield strength. The effects of reinforcing Mg by a powder metallurgy (PM) route and the application of biocompatible corrosion inhibitors (immersion in 0.1 and 1 M KF solution treatments, 0.1 M FST and 1 M FST, respectively) were analyzed in order to improve Mg mechanical and corrosion resistance, respectively. Open circuit potential measurements, polarization techniques (PT), scanning electrochemical microscopy (SECM) and electrochemical impedance spectroscopy (EIS) were performed to evaluate its corrosion behavior. SECM showed that the local current of attacked areas decreased during the F^- treatments. The corrosion inhibitory action of 0.1 M FST and 1 M FST in phosphate buffered solution was assessed by PT and EIS. Under the experimental conditions assayed, 0.1 M FST revealed better performance. X-ray photoelectron spectroscopy, energy dispersive X-ray and X-ray diffraction analyses of Mg(PM) with 0.1 M FST showed the presence of $KMgF_3$ crystals on the surface while a MgF_2 film was detected for 1 M FST. After fluoride inhibition treatments, promising results were observed for Mg(PM) as degradable metallic biomaterial due to its higher yield strength and lower initial corrosion rate than untreated Mg, as well as a progressive loss of the protective characteristics of the F^--containing film which ensures the gradual degradation process.

1. Introduction

One of the limitations of current internal fixation implants is the eventual release of toxic metallic ions and/or particles [1,2]. The concentration of ions released from different alloys used as orthopedic implants (cobalt, chromium, nickel, molybdenum, titanium, aluminum and vanadium ions) were reviewed by Sargeant and Goswami [3]. Metal ion levels may reach harmful values and cause adverse physiological effects such as cytotoxicity, genotoxicity, carcinogenicity, and metal sensitivity. These effects are reduced when screws, plates and pins that secure serious fractures are removed by a second surgical procedure after the tissue has healed. However, repeated surgery increases morbidity and health care system costs [4]. Another unfavorable effect of non-degradable implants is the adaptive bone remodeling that occurs in response to an altered mechanical environment following their insertion. This process is commonly referred to as "stress shielding" or stress transfer. Furthermore, pediatric permanent fixtures must be avoided because they cause an additional problem: the restriction of developmental bone growth.

In this context, implants of biocompatible metals such as Mg alloys seem to have a promising future. They have been proposed to avoid the harmful effects mentioned above since they are degradable (second surgery is prevented), their mechanical properties are closer to those of bone than other biometals, they reduce stress shielding and resulting osteopenia, and they are able to stimulate growth of new bone tissue [5–8]. Their degradation properties are also useful in the case of cardiovascular implants [9,10], particularly for preterm babies [11].

However, some negative issues should be solved before using Mg-based biomaterials; one of them is their excessively high degradation rate in body fluids [12–14]. Fortunately, the release of

☆ Part of the Thermec'2009 Biodegradable Metals Special Issue, edited by Professor Diego Mantovani and Professor Frank Witte.

* Corresponding author. Address: Instituto de Investigaciones Fisicoquímicas Teóricas y Aplicadas (INIFTA, CCT La Plata-CONICET), Facultad de Ciencias Exactas, Universidad Nacional de La Plata, Casilla de Correo 16, Sucursal 4, 1900 La Plata, Argentina. Tel.: +54 221 4257430; fax: +54 221 4254642.
E-mail address: mmele@inifta.unlp.edu.ar (M.A.F.L. de Mele).

1742-7061/$ - see front matter © 2009 Acta Materialia Inc. Published by Elsevier Ltd. All rights reserved.
doi:10.1016/j.actbio.2009.11.004

magnesium ions from corroding metal into biological media does not cause toxicity (local or systemic) and may even have beneficial effects on some of the biological components [7,8,15,16]. Nevertheless, alloy components may cause biocompatibility difficulties. In fact, most Mg alloys currently evaluated for biomedical use [12] were originally designed for industrial applications not always meeting biocompatibility requirements. Consequently, from the biological point of view, the use of pure Mg is more advisable than the majority of Mg alloys. However, the mechanical properties of pure Mg are not quite suitable for its use as internal fixation biomaterial: its typical yield strength is 55 MPa, quite lower than that of natural bone (e.g. femur ≈ 110 MPa) [4,17–20].

In order to improve the mechanical and corrosion resistance of pure Mg, we have analyzed the effects of reinforcing this metal by a powder metallurgy (PM) route [21] and the application of appropriate corrosion inhibitors [22–27]. Fluoride treatments have been extensively reported to improve the corrosion resistance of Mg and its alloys in industrial environments [22–28] and recently for medical use [2]. Among different inhibition treatments proposed, we selected that of immersion in a KF solution (fluoride solution treatment (FST)) since it is low-cost, non-toxic, simple and easily handled for biomedical applications. Fluoride-treated biomaterials have shown lower cytotoxicity level and better biocompatibility than controls [29]. However, treatment conditions must be selected so as to fulfill the requirements of Mg implants. A complex behavior is expected from a degradable implant for internal fixation: low corrosion during the initial period while the bone is healing, followed by a progressive increase of corrosion rate to achieve total degradation in a relatively short period after bone restoration.

The aim of this work was to evaluate the mechanical properties of powder metallurgy Mg (Mg(PM)) and assay different corrosion inhibition treatments in order to select the best method to provide an adequate degradation rate. With this purpose, treatments with different KF concentrations and immersion periods were assayed, and the properties of Mg(PM) samples before and after treatments were assessed by surface analysis, electrochemical tests, and microscopic observations.

2. Materials and methods

2.1. Materials

Mg powder (99.8%, 325 mesh) was supplied by Alfa Aesar. Powder was cold-pressed by slowly increasing pressure up to 310 MPa in a special die designed for this use. The resulting compact of 40 mm diameter was extruded at 420 °C (extrusion ratio = 16:1). The microstructure was examined by optical microscopy (Olympus BH2). Sample preparation consisted of grinding on SiC paper with increasingly finer grits, followed by mechanical polishing with 6 and 1 μm diamond paste, and final polishing using colloidal silica. The grain structure was revealed by subsequent etching using ethanol solution (100 ml), picric acid (1 g), acetic acid (2 ml), and water (5 ml). In order to determine the yield stress and ductility of the extruded Mg, dog-bone tensile samples of 10 mm gage length and $2 \times 4\ mm^2$ transversal section were machined from the center of the extruded bar with the tensile axis parallel to the extrusion direction (ED). These samples were tested at $10^{-3}\ s^{-1}$ constant strain rate at room temperature using an Instron testing machine.

Cylindrical samples (1 cm diameter) were cut from Mg(PM) rods. The lateral surfaces were covered by epoxy resin leaving a circular exposed area of 0.785 cm^2. The samples were ground and dry-polished with SiC papers of successively finer grit down to 1500 grit. Once polished, the samples were rinsed in ethanol and dried with nitrogen. For corrosion inhibition treatments, samples were placed horizontally on a Teflon cell [30] to form the conversion coating. Treated samples were then rinsed in ethanol and dried with nitrogen. The sample surface appearance was carefully examined by optical microscopy before and after the experiments so as to check color and texture uniformity of the conversion coating.

To improve their corrosion resistance Mg(PM) samples were treated in 0.1 M KF or 1 M KF solutions (0.1 M FST or 1 M FST, respectively) during different immersion periods from 1 h to 168 h (7 days). All solutions were prepared with ultrapure water by means of a Millipore Milli-Q system ($18.2\ M\Omega^{-1}$). Solutions employed in the experiments were: 0.1 M KF, 1 M KF, 8 g l^{-1} NaCl, and PBS (8 g l^{-1} NaCl, 0.2 g l^{-1} KCl, 0.2 g l^{-1} KH_2PO_4, 1.15 g l^{-1} Na_2HPO_4). Analytical grade reagents were used in all cases.

2.2. Characterization of fluoride conversion coating (SECM, SEM, XDR, and XPS)

The surface topography was studied before and during F^--treating using scanning electrochemical microscopy (SECM) (Sensolytics) equipped with a 10 μm platinum tip as probe, Ag/AgCl/KCl reference electrode, and a platinum wire as counter electrode, all placed within a polytetrafluoroethene cell. Mg(PM) specimens were mounted horizontally facing upwards. Open circuit potential (E_{ocp}) experiments were performed in 0.1 M KF solution as background electrolyte. The scan rate of the microscope tip over the specimen surface was 10 μm s^{-1} in unidirectional lines, with 5 μm separation between line scans. The maps were generated with the tip located ~10 μm from the Mg(PM) surface.

The Mg(PM) sample previously corroded in 8 g l^{-1} NaCl for 1 h was dipped into the SECM electrolytic cell with 0.1 M KF aerated solution. The topography was analyzed in a feedback mode using O_2 dissolved in solution as electrochemical mediator. The oxygen related current was recorded directly by the SECM-tip set at −0.70 V. At this potential, O_2 reduction occurs and the current magnitude at the microelectrode is dependent on the O_2 concentration. In turn, O_2 concentration at the microelectrode surface depends on the local O_2 concentration within the diffusion layer, which is affected by the O_2 concentration of the bulk solution. After recording the steady-state current $i(\infty)$, with the tip far from the Mg(PM) surface, the height of the tip above the sample was adjusted until $i/i(\infty)$ reached a value of 0.25.

A Philips XL30 scanning electron microscope was used for SEM observations, coupled to the energy dispersive X-ray (EDX) DE4i analyzer. Phases in the coating were determined by X-ray diffractometry (X'Pert PRO XRD, Panalytical) at a glancing angle of 0.5°, 0.7° and 1° using the CuK_α line generated at 40 mA, 45 kV. Start position ($2\theta°$) 20.0100; end position ($2\theta°$) 69.9900; step size ($2\theta°$) 0.0200; scan step time (s) 2.0000. In order to determine sample composition and identification, the PDF-4+ database (ICDD) was used. Occasionally, surface deposits were detected using a FEG-SEM, Jeol-JSM 6500, F analytic field emission gun with an Oxford EDX microanalysis system.

The surface composition was analyzed by X-ray photoelectron spectroscopy (XPS) [31]. Photoelectron spectra were obtained with a VG Escalab 200R spectrometer equipped with a hemispherical electron analyzer (50 eV pass energy) and a MgK_α ($h\nu$ = 1254.6 eV, 1 eV = 1.6302×10^{-19} J) X-ray source, powered at 120 W, background pressure below 2×10^{-8} mbar, calibrated relative to the C 1s peak at 284.9 eV. The raw data were used with no preliminary smoothing. Symmetric Gaussian–Lorentzian product functions were employed to approximate the shapes of the fitting compo-

nents. Atomic ratios were computed from experimental intensity ratios and normalized by atomic sensitivity factors [32].

2.3. Electrochemical measurements

An electrochemical cell with a three-electrode setup was used. A platinum wire (99.99% purity) served as auxiliary electrode. All potentials are quoted with respect to the Ag/AgCl/KCl reference electrode. The exposed area of the working electrode (Mg(PM) disk) was 0.785 cm^2 for all the experiments. Solutions were maintained at 37 ± 0.5 °C and deaerated with pure nitrogen in the case of polarization curves and transient currents.

A TEQ-02 potentiostat was used for potentiodynamic polarization curves from −1.88 V up to different anodic limits at 10 mV s^{-1}. Lower scan rates could not be employed since they provide very unstable measurements when Mg(PM) is used. E_{ocp} vs. time values were also recorded. Additionally, transient currents were measured at fixed potentials (E_{ocp} + 30 mV and E_{ocp} + 50 mV, vs. Ag/AgCl/KCl).

Each electrochemical impedance spectroscopy (EIS) experiment was carried out at E_{ocp} by applying a sinusoidal wave of 10 mV amplitude in 10^5 Hz to 10^{-2} Hz frequency range, logarithmically spaced (120 data points per decade) using an Autolab/PGSTAT10 potentiostat from Eco-Chemie.

3. Results

3.1. Mg(PM) microstructural characteristics and tensile stress

The microstructure of Mg(PM) is shown in Fig. 1. Significant grain refinement was obtained by this PM processing route due to the dynamic recrystallization during hot extrusion. Grain sizes are heterogeneous, around 5 μm or smaller, with small oxide particles attached to the grain boundaries. These particles come from the fracture during extrusion of the oxide film that covers the original Mg powder.

Fig. 2 shows the true stress–strain curve for Mg(PM) samples. This material shows 2% ductility, offset stress (at 0.2% strain) of 280 MPa and a tensile stress of 320 MPa. Three tensile curves corresponding to the widely used AZ31 Mg alloy in the form of rolled sheet [21], with 2 μm and 55 μm grain sizes, and to pure cast magnesium (grain size in the order of millimetres) are also shown in this figure.

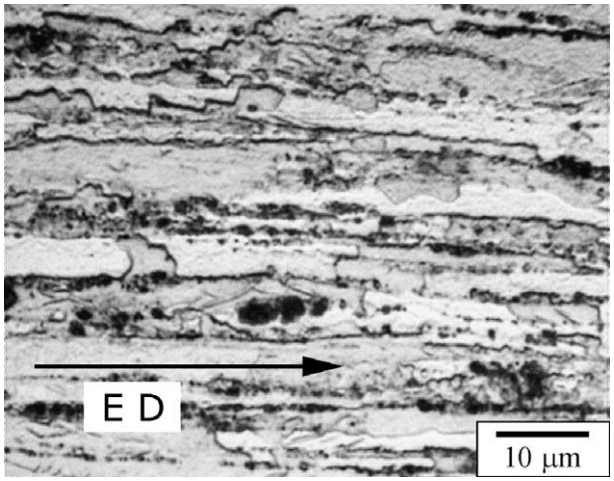

Fig. 1. Optical micrograph showing the microstructure of the Mg(PM) extruded bar. ED = extrusion direction.

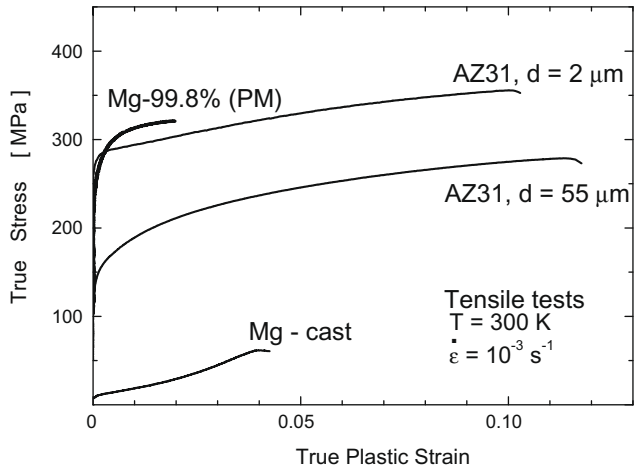

Fig. 2. True stress–strain curve of the Mg(PM) material compared with the AZ31 magnesium alloy [21].

3.2. Conversion coating formation

3.2.1. Characterization of fluoride-coated surface

The Mg(PM) samples were treated with F^--containing solution to form a protective conversion coating. After 0.1 M FST treatment, a stable film with F^--containing compounds was formed and its thickness increased with time. The SEM microphotograph (Fig. 3) and EDX analysis showed the presence of $KMgF_3$ cubic crystals similar to those previously reported for AZ91 Mg alloy [24]. The EDX analysis in different areas of the substrate revealed that the atomic percent of fluor on the surface increased when immersion time was longer (Table 1).

The X-ray diffraction (XRD) pattern for F^--coated Mg(PM) (Fig. 4) confirmed the presence of this $KMgF_3$ on Mg substrate. The average $KMgF_3$ crystallite size at 25 °C was calculated according to the line broadening of the diffraction peaks, applying Scherrer's equation (average value = 318 Å).

In the case of 1 M FST-treated samples, the resulting film was characterized by X-ray photoelectron spectroscopy (XPS). XRD could not be used due to the particular characteristics of the coating. Fig. 5 shows the high-resolution spectrum for Mg 2p binding energy at the Mg(PM) surface with 1 M FST, after different immersion times (from 5 h to 7 days). The Mg 2p signal (50.7–51.1 eV) and F 1s (684.2–684.8 eV) proved that the chemical composition of the film formed was MgF_2 for each immersion time (Table 2),

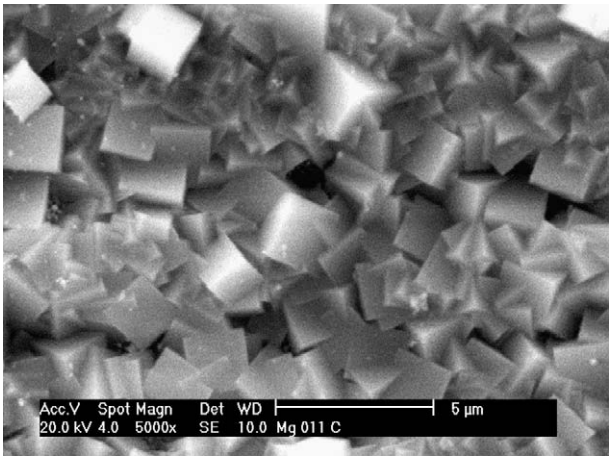

Fig. 3. SEM microphotograph of Mg(PM) after 0.1 M FST for 7 days.

Table 1
EDX analysis of Mg(PM) after 0.1 and 1 M FST with different immersion periods.

Immersion time	*F* (at.%)	Average value (at.%)
Treatment: 0.1 M FST		
1 h	6.46	6.23
	6.01	
5 h	11.54	10.67
	10.33	
	10.14	
22 h	19.68	18.16
	17.88	
	16.94	
Treatment: 1 M FST		
1 h	10.78	12.00
	10.74	
	13.14	
	13.35	
5 h	9.47	8.46
	8.24	
	7.67	
22 h	11.38	12.02
	12.66	

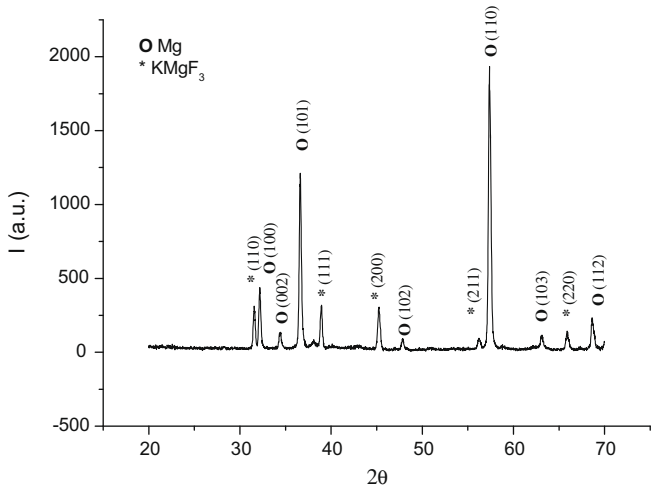

Fig. 4. XRD spectrum of Mg(PM) after 0.1 M FST for 7 days (glancing angle = 1°).

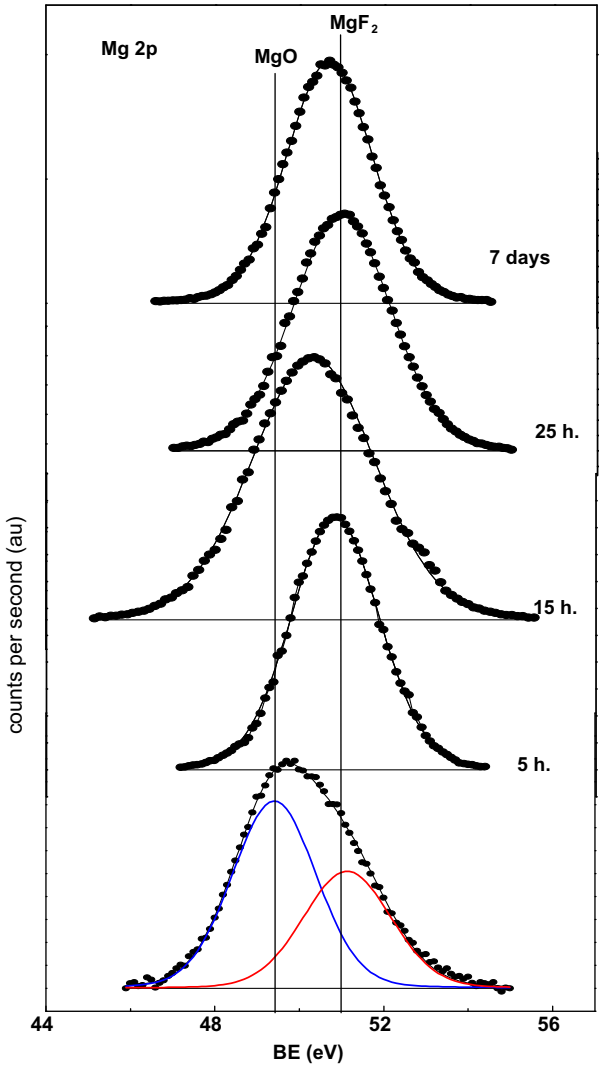

Fig. 5. XPS high-resolution Mg $2p_{3/2}$ spectrum at the surface of Mg(PM) after 1 M FST at different immersion times.

although an atomic ratio of Mg to F equal to 0.5 was only reached at long exposure times (Table 2, last column). The analysis of a reference sample with Mg oxide (Mg 2p 49.6 eV) and Mg fluoride (Mg 2p 51.1 eV) is also shown for comparison. When Mg bonded to fluoride, the Mg 2p core level binding energy shifted to 1.5 eV higher in energy. These results are in agreement with those obtained by Chiu et al. [2] for Mg in hydrofluoric acid. However, other authors [20] showed that it is impossible to discriminate between oxide and hydroxide forms since the Mg 2p peak position is similar for both compounds. Nevertheless, the O 1s peak corresponding to MgO located at an absolute BE around 531 eV, and the O 1s peak corresponding to OH species located near 533.2 eV allow us to distinguish between them. In our study, oxygen originating from adventitious C—O-containing compounds was found but not from Mg hydroxides or oxides as suggested by Verdier et al. using HF [22]. The high-resolution O 1s spectrum showed the separation of O 1s band in two components: at 531.7–532.2 eV and 533.7 eV corresponding to C=O and C—O bonds, respectively. The high-resolution C 1s spectrum can be resolved in three peaks: one at 284.8 eV representing carbons in a hydrocarbon environment (C—C, C—H) and the others at 286.4 and 288.4 eV representing carbons in C=O and O—C=O bond, respectively (spectrum not shown).

Mass increase per unit area of Mg(PM) as a function of time during 1 M FST is depicted in Fig. 6. The graph shows a monotonic increase in mass and hence, according to XPS data, the growth of the MgF_2-containing film with immersion time during 1 M FST. The average increase was 2.63 $\mu g\, h^{-1}$. In agreement, a monotonic increase in the specific mass (mass/area) was reported for the Mg samples immersed in HF [2] for short periods. However, the authors noticed that the growth rate slowed down for longer immersion periods while a nearly constant slope was found for the case of 1 M FST with KF solutions.

3.2.2. Open circuit potential measurements

E_{ocp} vs. time of Mg(PM) was measured during the treatments 0.1 and 1 M FST (Fig. 7). A sharp increase in E_{ocp} from −1.8 V to −0.3 V could be observed in the 1 M KF solution during the first hours after immersion. Then, E_{ocp} showed a slow increase up to ca. −0.1 V after 7 days of immersion. On the contrary, when Mg(PM) was immersed in 0.1 M KF (Fig. 7) the potential increased more slowly than for the case of 1 M KF solutions, reaching −0.9 V at the end of the test time.

Table 2
The binding energy (eV) for the elements on Mg(PM) after 1 M FST with different immersion periods.

Immersion time	K $2p_{3/2}$	F 1s	Mg 2p	O 1s	Mg/F at.
5 h	292.7	684.6	50.8	531.9 533.7	0.36
15 h	292.8	684.8	50.9	531.8 533.4	0.39
25 h	292.8	684.2	51.0	531.7 533.6	0.38
7 days	292.8	684.4	50.7	532.2 533.7	0.49
MgO + MgF_2	293.0	684.8	49.6 51.1	530.9 532.8	

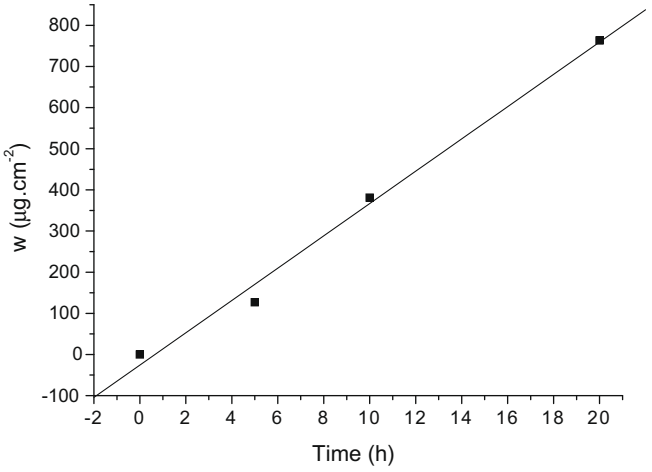

Fig. 6. Mass gain of Mg(PM) samples after 1 M FST with different immersion times.

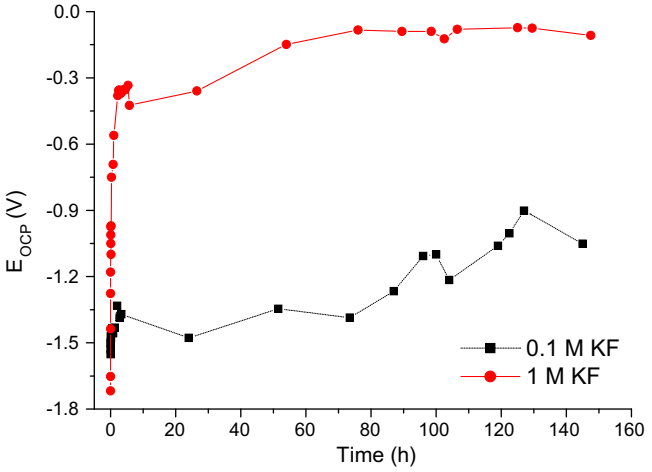

Fig. 7. Open circuit potential (E_{ocp}) vs. time of Mg(PM) during 0.1 and 1 M FST.

3.3. Electrochemical characterization of the conversion coating

3.3.1. SECM characterization in F^--containing medium

F^--action during 0.1 M FST treatment was followed by SECM (Fig. 8a). This electrochemical imaging technique allows the visualization of spatially confined variations in the chemical reactivity. Previous to SECM measurements the Mg(PM) sample was immersed in 8 g l^{-1} NaCl. During this process localized corrosion (micropits) occurred (Fig. 8b). The height of current peaks in Fig. 8a is related to the activity within the pits. At the beginning of the scanning on the 2000 µm × 600 µm *X–Y* plane, the local current values simulated the topography of the surface, initially with active pits. However, due to the protective effect of the background electrolyte (0.1 M KF), lower variation in the current values were progressively detected during the successive scans, giving rise to approximately constant current values at the end of the experiment, associated with the flat image of a passive surface. SECM showed locally the effective action of the F^- ions to inhibit localized corrosion in the absence of Cl^- ions. This sensitive measurement cannot be applied to Mg(PM) in the presence of chloride ions due to the formation of hydrogen bubbles.

3.3.2. Potentiodynamic and potentiostatic electrochemical measurements in PBS

Anodic polarization curves for active metals such as Mg frequently depict the formation of a slightly protective layer of corrosion products on the surface, which yields pseudo-passivation. In Fig. 9 typical polarization curves obtained for Mg(PM) in PBS can be observed. The curves show an imperfect passivation region during the anodic run. In all cases, when pitting begins, a sharper increase in current is recorded. Local dissolution of the metal occurs where the protective film is broken. Bubbles associated with hydrogen evolution become more intense as the applied anodic polarization potential increases.

In order to select an adequate treatment to guarantee a suitable degradation rate for the metal, several conditions were assayed using 0.1 M FST (Fig. 9a) and 1 M FST (Fig. 9b) with different immersion times (between 1 h and 20 h).

According to the potentiodynamic measurements, the most protective action for 0.1 M FST samples immersed in PBS was obtained from the longest immersion time, characterized by the most anodic breakdown potential. Lower protective action in PBS was found for 1 M FST samples with more cathodic breakdown potentials in all cases. Unexpectedly, the breakdown potentials for 1 M FST samples corresponding to 5 h and 20 h were more cathodic than that for 1 h.

It is worth noting that when Mg(PM) samples were immersed in PBS solution, that is, in the absence of fluoride ions, E_{ocp} values decreased due to the progressive dissolution of the F^--containing layer (not shown).

Transient currents measured at a potential 30 mV more anodic than the E_{ocp} value (E_{ocp} measured 3 min after immersion in PBS) showed (Fig. 10) that after 1 h–1 M FST the current remained at higher values than those for 1 h–0.1 M FST. In the case of 20 h–0.1 M FST treatment, the passivity breakdown could be observed after an induction time period that was shorter if the potential value was more anodic (compare the curves at +30 mV and +50 mV more anodic than the E_{ocp} value).

3.3.3. Electrochemical impedance spectroscopy (EIS) results in PBS

Electrochemical impedance spectroscopy was performed in PBS at the open circuit potential E_{ocp} on Mg(PM) after 1 h–0.1 M FST and 20 h–0.1 M FST and 20 h–1 M FST. The impedance dates of the samples with 0.1 M FST acquired by EIS are shown in both the Nyquist and Bode plots in Fig. 11. The Nyquist diagrams (imaginary part Z″ vs. real part Z′) show, in general, two frequency regions (Fig. 11a and c). At high frequencies the semicircle parts correspond to the charge transfer resistance limiting process associated with $KMgF_3$ salt film/electrolyte interface (R_{CT}). Its intercept with the real axis, at high frequencies, corresponds to electrolyte resistance (R_S). At low frequency, an inductive behavior was observed, usually associated with ion adsorption–desorption in a corrosion process. The experimental capacitance was calculated in the

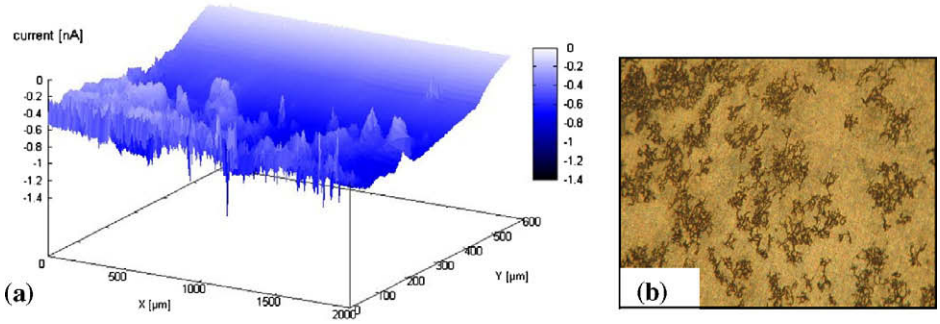

Fig. 8. (a) Topographic map generated by SECM of a Mg(PM) sample (previously immersed in 8 g l^{-1} NaCl for 1 h) during 0.1 M FST. Tip potential = −0.70 V. (b) Optical microphotograph of the electrode at the beginning of the scanning.

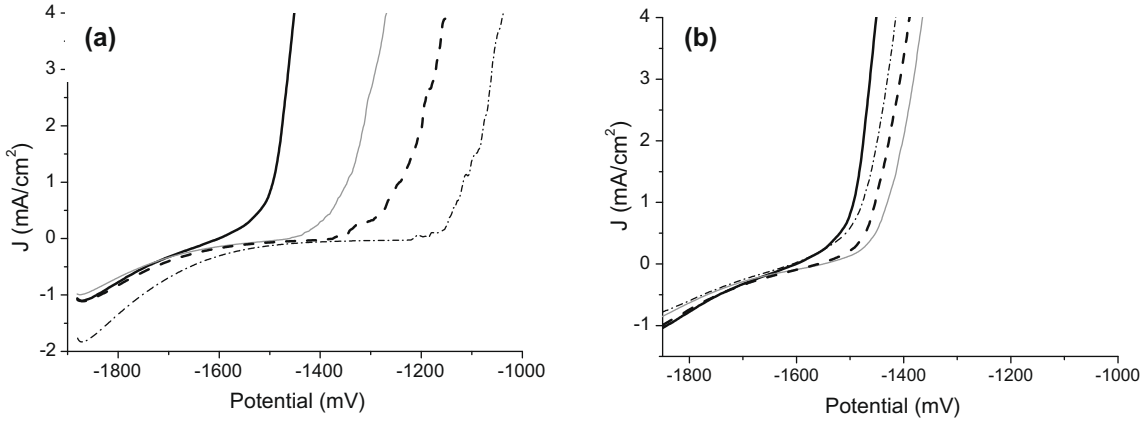

Fig. 9. Potentiodynamic anodic polarization curves recorded at 10 mV s^{-1} in PBS: (—) without pre-treatment, and after (a) 0.1 M FST; (b) 1 M FST for (—) 1 h, (- - -) 5 h and (-·-·-) 20 h in KF solutions.

medium-frequency range by means of the fixed frequency method. The frequency was selected in order to obtain a maximum value of φ and the capacitance was calculated as $C = 1/(2\pi f_i Z_i)$, where Z_i is the imaginary part of the impedance at fixed frequency, f_i (Table 3).

The impedance modulus Bode diagrams (Fig. 11b and d) revealed a plateau at high frequencies. The impedance value at this region, with $\varphi = 0$, gave the electrolyte resistance for each case. At decreasing frequencies (10^3 Hz–10 Hz), the slope (−0.70) could be attributed to one capacitor in parallel with a resistance corresponding to the $KMgF_3$ salt film/electrolyte interface, being the phase angle close to −60°. At the lowest frequency range, the phase angle is close to 0°, corresponding to a plateau in the impedance modulus vs. frequency plot where the total resistance of the circuit can be obtained.

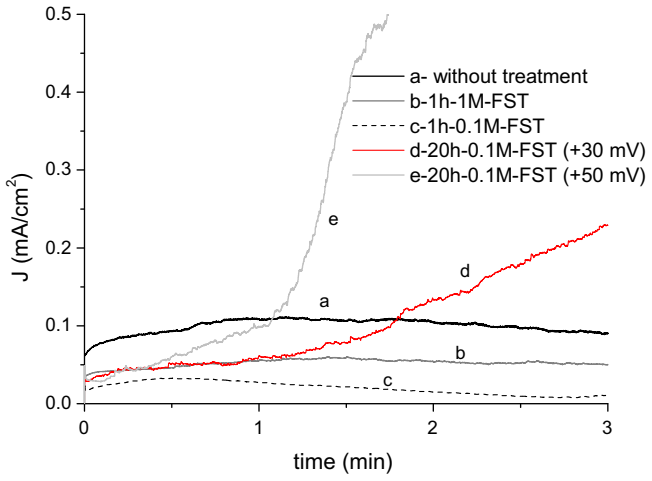

Fig. 10. Transient currents measured at E_{ocp} +30 mV (a–d) and E_{ocp} +50 mV in PBS.

Impedance data acquired by EIS of Mg(PM) samples with 20 h–1 M FST are also shown in both the Nyquist and Bode plots in Fig. 12. The Nyquist plot shows a capacitive arc at high and medium frequencies (Fig. 12a). For simplicity, one might take the real impedance at which the imaginary part vanishes for the capacitive part to be the charge transfer resistance R_{TC} and relate it to the corrosion resistance (424 Ω cm^2). The impedance modulus vs. frequency plot (Fig. 12b) shows a slope value close to 0.5 (−0.57) for frequencies between 3 Hz and 58 Hz, which confirms the presence of a one time constant. At this frequency range the phase angle shows a clear sharp maximum at −42°. It is possible to calculate the R_S from the impedance modulus value at the highest frequency (157 Ω). The experimental results are shown in Table 3.

3.4. Surface characterization of F^-- treated Mg(PM) degradation after immersion in PBS

Localized corrosion was observed when Mg(PM) samples were immersed in PBS, after both 0.1 and 1 M FST treatments (Fig. 13). However, higher and faster degradation occurred after 1 M FST with a parallel decrease in the F content of the protective layer (compare values in Tables 4 and 5). Circular deposits of corrosion products were detected by SEM. The distribution map of different components was made by EDX analysis (Fig. 14). After both treatments, O and P surface concentrations increased in the circular

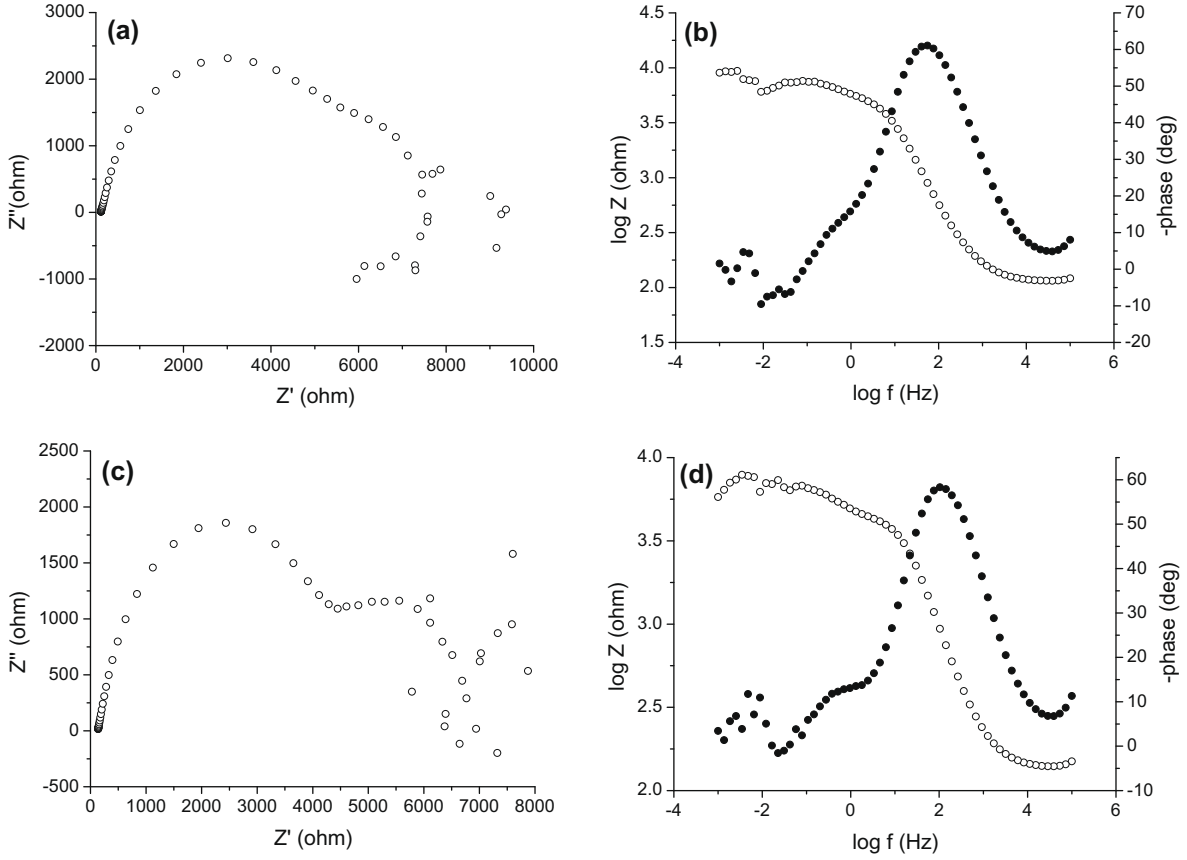

Fig. 11. EIS spectra, Nyquist and Bode plots of Mg(PM) immersed in PBS after (a and b) 1 h–0.1 M FST and (c and d) 20 h–0.1 M FST.

Table 3
Experimental parameters obtained from EIS plots of Mg(PM) with 0.1 and 1 M FST.

Treatment	Immersion period	R_s (Ω)	C (F cm^{-2})	R_{CT} (Ω cm^2)
0.1 M FST	1 h	138	1.39×10^{-5}	1769
0.1 M FST	20 h	112	2.85×10^{-5}	2237
1 M FST	20 h	157	17.2×10^{-5}	424

deposits (Tables 4 and 5). Additionally, C was also detected over the surface with higher percentage in the case of 0.1 M FST.

4. Discussion

Pure Mg has been proposed as a potential degradable biomaterial to avoid the disadvantages of non-degradable internal fixation implants and the toxicity of some alloy elements [8,12]. Unfortunately, it shows low yield strength and excessively high corrosion rate. Herein, we have analyzed the application of biocompatible corrosion inhibition treatments to pure Mg processed by a powder metallurgy route (Mg(PM)) to improve its mechanical properties and corrosion resistance.

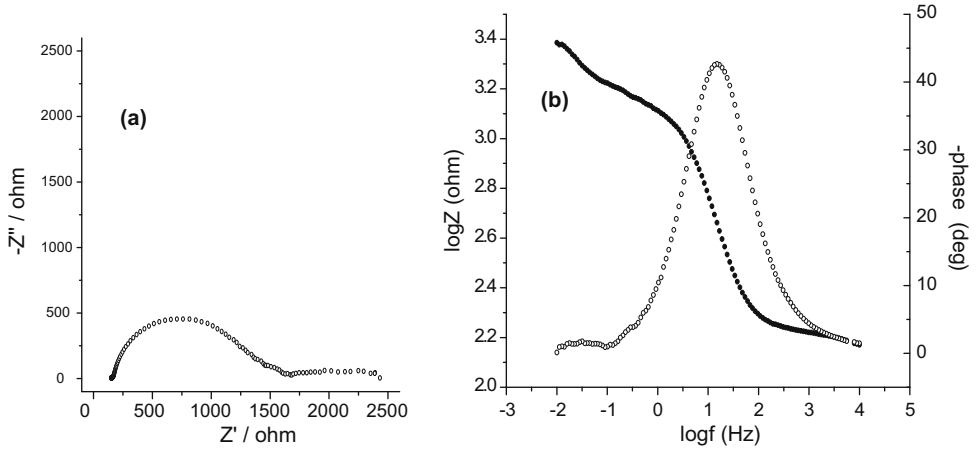

Fig. 12. EIS spectra, Nyquist and Bode plots of Mg(PM) immersed in PBS after 20 h–1 M FST.

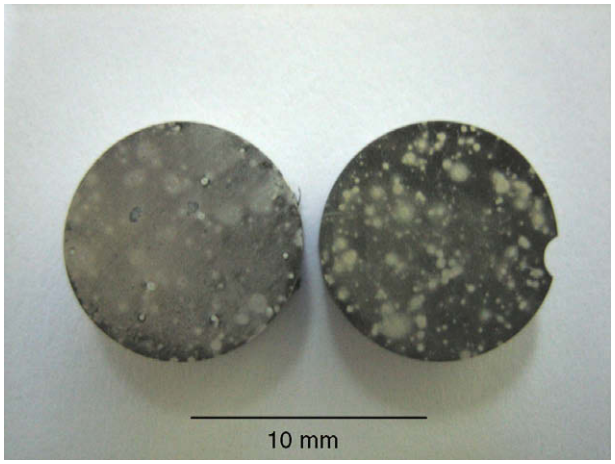

Fig. 13. Mg(PM) after 1 h–0.1 M FST (left) and 1 h–1 M FST (right) followed by 20 min immersion in PBS.

Table 4
EDX analysis of Mg(PM) after 1 h–0.1 M FST followed by 20 min in PBS.

Element	Region A		Region B	
	wt.%	at.%	wt.%	at.%
C K	3.25	5.42	4.91	8.97
O K	33.86	42.31	7.85	10.76
F K	6.05	6.36	6.51	7.52
Na K	0.97	0.85	0.08	0.08
Mg K	50.95	41.90	80.13	72.32
P K	4.93	3.18	0.41	0.29
Cl K	−0.09	−0.05	−0.01	0.00
K K	0.08	0.04	0.11	0.06
Total	100.00		100.00	

Table 5
EDX analysis of Mg(PM) immersed for 1 h in 1 M FST followed by 20 min in PBS.

Element	Region A		Region B	
	wt.%	at.%	wt.%	at.%
C K	2.18	3.78	2.20	4.21
O K	28.78	37.46	4.50	6.46
F K	6.62	7.26	6.91	8.35
Na K	1.09	0.99	−0.07	−0.07
Mg K	52.48	44.96	84.61	79.93
P K	6.07	4.08	0.19	0.14
Cl K	0.00	0.00	−0.10	−0.06
K K	2.78	1.48	1.75	1.03
Total		100.00		100

4.1. Improvement of Mg mechanical properties by powder metallurgy

Mg(PM) benefits from the contribution of various strengthening mechanisms [33]. First, a large grain size refinement is observed in comparison with cast pure Mg with grain sizes of several millimetres, which increase yield stress. Hall–Petch law [34] provided the relation between yield stress and grain size for Mg. Secondly, there is a contribution of Mg oxides dispersion resulting from the rupture of the oxide film covering Mg powder during extrusion which produces a mechanical reinforcement through the Orowan mechanism [33,35]. Additionally, Pérez et al. [35] showed that the considerable crystallographic texture, developed during the extrusion process, significantly contributes to the tensile strength. As is expected for a PM material, there is a reduction in ductility compared to wrought materials.

As a result of these microstructural improvements, the material employed in the present work has a yield strength of 280 MPa, considerably higher than that of pure cast magnesium and close to the values obtained for the widely used AZ31 Mg alloy [21], avoiding the release of alloy elements such as Al.

4.2. Inhibition of Mg(PM) corrosion by F^- treatments

When selecting an inhibitory treatment to protect Mg(PM) from corrosion, two precautions should be taken into account: (i) it should be strong enough to preserve the implant during tissue healing; (ii) it should progressively lose the protective properties to allow the degradation of the implant after bone repair [2].

Among the inhibition treatments proposed [36] we chose immersion in KF solution since it is low in cost, simple, biocompatible, and less dangerous and more easily handled than HF treatments [29]. However, several assays had to be made in order to select the proper treatment to satisfy implant requirements. Two fluoride concentrations were employed (0.1 M and 1 M KF), and different immersion periods were tested (1 h and 20 h).

After 0.1 M FST, XRD analysis revealed the formation of $KMgF_3$, structured as a protective layer on the surface. SEM and EDX analyses showed the presence of $KMgF_3$ cubic crystals. EDX data proved that F content increases with time together with the shielding characteristics of the layer that, according to electrochemical measurements, seems to provide a sealing effect. Thus, E_{ocp} vs. time plot depicted an increase in the potential up to −0.9 V during 0.1 M FST treatment (Fig. 6).

On the other hand, for 1 M KF solutions E_{ocp} increased up to −0.1 V while the weight of the substrate increased with time during the treatment (Fig. 6). In parallel, Mg(PM) mass increased. However, mass increase cannot be exclusively associated with the formation of F^--containing compounds: oxygen and carbon-containing species may also be present. Accordingly, the composition of the protective coating changed progressively including other products. XPS data showed that oxygen atoms were probably bonded to C (C=O). In agreement, Baril et al. [38] reported the adsorption of CO_2 from the atmosphere on Mg-based substrates. Consequently, HCO_3^- and CO_3^{2-} may form carbonate-containing corrosion products on the surface. The XPS analysis of 1 M FST samples showed that the MgF_2 layer was the only Mg-containing product within the thin external layer analyzed by XPS. However, $Mg(OH)_2$ and $Mg(OH)_xF_{2-x}$ may also be present in the inner layers [22].

SECM findings showed locally the strong action of F^- ions to reduce the corrosion rate of the previously corroded Mg(PM) sample, confirmed by potentiodynamic and potentiostatic results in PBS.

4.3. Corrosion behavior of F^--treated samples in PBS

Polarization curves in PBS indicated that the breakdown potential increased at longer immersion times in 0.1 M KF solution (Fig. 10a) and consequently, the substrates seemed to be less susceptible to localized attack after 20 h–0.1 M FST. However, transient current measurements revealed that when the sample remained at a constant potential 30 mV more anodic than the E_{ocp}, the passivity breakdown occurred after an induction time in the order of minutes. This induction time was shorter when the constant potential applied was more anodic. It seems that after the longest treatment with 0.1 M KF, the protective layer became more compact but more labile to the localized attack.

At this point, it is interesting to analyze why the values of breakdown potential measured by potentiodynamic techniques were more anodic than those obtained by potentiostatic assays. It should be considered that when potentiodynamic measurements at 10 mV s^{-1} scan rate are performed, the potential shifts continu-

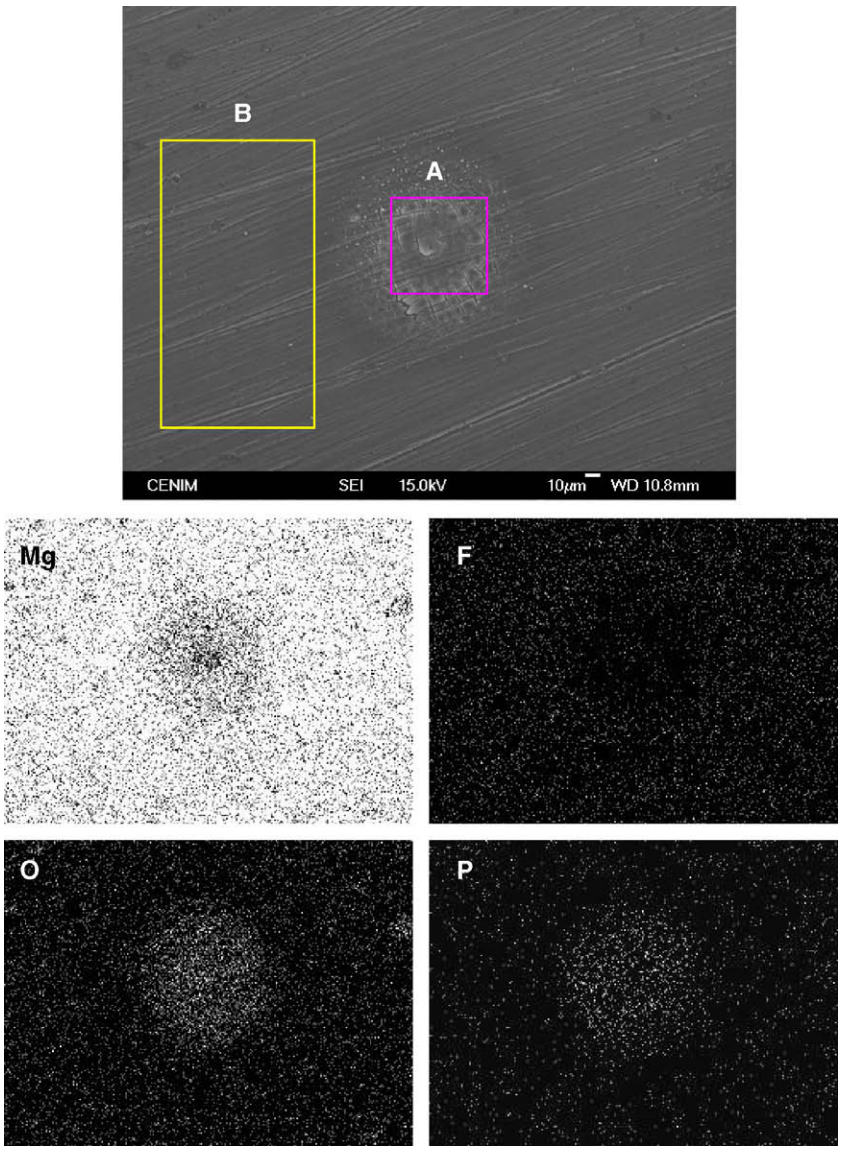

Fig. 14. SEM microphotograph and EDX compositional maps of different elements (Mg, F, O and P) of Mg(PM) surface with 1 h–0.1 M FST followed by 20 min immersion period in PBS. Region A and B includes the areas with and without precipitated products, respectively (see EDX analysis in Tables 4 and 5).

ously to more anodic values (300 mV in 30 s). Consequently, the passivity breakdown that takes place after a certain induction time is detected at more anodic potential values than under potentiostatic conditions (transient current measurements).

A different behavior and lower effectiveness were found for 1 M FST treatment. The increase of the immersion time in the 1 M KF solution which implies an increase of the E_{ocp} up to −0.4 V (after 20 h) and the formation of a heterogeneous layer (XPS data) resulted in neither a significant increase of F content during the first 20 h, nor a better protective characteristic of the conversion coating. Thus, breakdown potentials were in all cases lower than for 0.1 M FST (Fig. 9a and b). Electrochemical results presented here are in agreement with those previously reported for Mg alloys in halide media [24], which also demonstrated that fluoride treatment contributes to the formation of a surface salt film with inhibitory effects that strongly depend on the anion concentration, reaching a maximum beyond which the F^- ion level adversely affects the corrosion resistance.

Interestingly, the percentage of C-containing compounds increased at longer exposure times, with higher C content in 0.1 M FST samples. In this regard, it has been demonstrated that the presence of $NaHCO_3$ improves the corrosion resistance of Mg immersed in Hank's solution [38]. Consequently, the higher corrosion resistance of the layer formed in 0.1 M FST could be associated with the inclusion of C-containing compounds into the conversion coating.

EIS spectra also showed significant differences between the behavior of the Mg(PM) treated with 1 and 0.1 M FST. For 1 h–0.1 M FST and 20 h–0.1 M FST at high frequencies, the Nyquist plot showed a capacitive behavior associated with $KMgF_3$ salt film/electrolyte interface with 1769 and 2237 Ω cm^2 as the experimental values for R_{CT}. The R_{CT} for F^- coating formed in 0.1 M KF was significantly higher than that for the film formed in 1 M KF (2237 cm^2 for 20 h–0.1 M FST and 424 cm^2 for 20 h–1 M FST) which could be related with the higher corrosion resistance of Mg(PM) with 0.1 M FST. The structural characteristics of the $KMgF_3$ layer, together with the higher C content, seemed to confer better protection than the film formed during 1 M FST. However, according to transient current measurements, the most resistant layer formed after 20 h immersion in 0.1 M KF was more labile to the localized attack than that formed after 1 h immersion.

After immersion in PBS, Mg(PM) treated with 20 h–1 M FST showed an impedance modulus vs. frequency plot with a slope value close to −0.5, indicating the diffusion control of the corrosion process which could be related to phosphate precipitation. Microphotographs show small circular regions where high P and O contents were detected by EDX (Fig. 14). The local pH change associated with hydrogen evolution during the localized attack could favor the precipitation of phosphates close to this cathodic area, according to the P map in Fig. 14.

Hydrogen evolution does not seem to affect biocompatibility of Mg-based biomaterials [5], although it may be disadvantageous, particularly for cardiovascular applications.

4.4. Variable corrosion resistance of F^--treated samples

A variable resistive behavior of Mg(PM) with FST over time is appropriate for degradable implants since it provides initial corrosion protection, allowing the implant to preserve its mechanical integrity while the bone is healing. Subsequently, a higher corrosion rate favors biomaterial dissolution. Among degradable biomaterials pure Mg presents an additional advantage: this dissolution is not accompanied by the release of other metals, as in the case of Mg alloys [2,38,39].

We will now analyze the variation of Mg(PM) corrosion resistance during 1 and 0.1 M FST treatments, and after immersion in PBS. The interaction of F^- with hydrogen ions could explain the high corrosion resistance of the F^--containing coatings when F^- ions are present (during 0.1 and 1 M FST). According to local pH measurements made on corroding Mg [40], while pH at the interface of the cathodic area is increased by hydrogen ion consumption it decreases in the anodic area due to the hydrolysis of metal ions from the corrosion reaction. F^- ions are highly electronegative [25], with strong binding energy to hydrogen, leading to HF_2^-, $H_2F_3^-$ and $H_3F_4^-$ layer formation on the surface. This adsorption layer may retard the reaction between the hydrogen ion and the substrate that leads to corrosion. However, when F^--treated Mg(PM) is immersed in the PBS (F^--free environment), Cl^- ions begin to adsorb strongly on the metal surface [20,24,28], displacing F^- ions from the protective layer which progressively loses its corrosion resistance. In this regard, the high incorporation of C-containing compounds (Table 4) by the $KMgF_3$ layer formed during 0.1 M FST benefits the corrosion-resistive behavior of Mg(PM) against chloride action for a longer time [37].

In relation to clinical application of Mg(PM), the inhibitory treatment to protect Mg(PM) from corrosion should be strong enough to preserve the implant during tissue healing. In a simulated biological environment the degradation rate of Mg(PM) with 1 h–0.1 M FST in PBS is still high in relation to the healing period of the tissues. However, when Mg(PM) is implanted, its dissolution rate may be slightly lower due to the restriction of ion diffusion towards the surrounding tissue [41].

5. Conclusions

Mechanical properties of pure Mg were improved using a PM route. Appropriate yield strength values were obtained for Mg(PM) as degradable implant material, avoiding the use of alloy elements that may be toxic.

Mg(PM) corrosion resistance was also improved by treatments with KF solutions. These assays are low-cost, easily handled and quite simple, and produce variable resistive behavior, suitable for degradable implants. Electrochemical tests revealed that Mg(PM) with 0.1 M KF treatment evidenced higher corrosion resistance than with 1 M KF treatment. However, experimental conditions must be upgraded in order to extend the action of the protective layer to allow complete tissue healing.

Acknowledgements

This work was financially supported by Consejo Nacional de Investigaciones Científicas y Técnicas (CONICET) (PIP 6075), Agencia Nacional de Promoción Científica y Técnica (PICT 0533225), Universidad Nacional de La Plata/Facultad de Ingeniería (Grant No. 11-I129), Grant Nos. CTQ2005-087-C02-01 and CTQ2008-05775/BQU, and MAT 2006-02672 (Ministerio de Educación y Ciencia, Spain).

Appendix A. Figures with essential color discrimination

Certain figures in this article, particularly Figs. 5, 7, 8, 10, 13 and 14, are difficult to interpret in black and white. The full color images can be found in the on-line version, at doi: 10.1016/j.actbio.2009.11.004).

References

[1] Pietrzak WS, Sarver D, Verstynen M. Bioresorbable implants—practical considerations. Bone 1996;19:109S–19S.
[2] Chiu KY, Wong MH, Cheng FT, Man Hc. Characterization and corrosion studies of fluoride conversion coating on degradable Mg implants. Surf Coat Tech 2007;202:590–8.
[3] Sargeant A, Goswami T. Hip implants—Paper VI—ion concentration. Mater Des 2007;28:155–71.
[4] Staiger MP, Pietak AM, Huadmai J, Dias G. Magnesium and its alloys as orthopaedic biomaterials: a review. Biomaterials 2006;27:1728–34.
[5] Witte F, Kaese V, Haferkamp H, Switzer E, Meyer-Lindenberg A, Wirth CJ, et al. In vivo corrosion of four magnesium alloys and the associated bone response. Biomaterials 2005;26:3557–63.
[6] Witte F, Fisher J, Nellesen J, Crostack H-A, Kaese V, Pisch A, et al. In vitro and in vivo corrosion measurements of magnesium alloys. Biomaterials 2006;27:1013–8.
[7] Gruhl S, Witte F, Vogt J, Vogt C. Determination of concentration gradients in bone tissue generated by a biologically degradable magnesium implant. J Anal Atom Spectrom 2009;24:117–248.
[8] Li L, Gao J, Wang Y. Evaluation of cyto-toxicity and corrosion behaviour of alkali-heat-treated magnesium in simulated body fluid. Surf Coat Tech 2004;185:92–8.
[9] Mani G, Feldman MD, Patel D, Agrawal CM. Coronary stents: a materials perspective. Biomaterials 2007;28:1689–710.
[10] Heubliein B, Rohde R, Kaese V, Niemeyer M, Hartung W, Haverich A. Biocorrosion of magnesium alloys: a new principle in cardiovascular implant technology. Heart 2003;89:651–6.
[11] Zartner P, Cesnjevar R, Singer H, Weyand M. First successful implantation of a biodegradable metal stent into the left pulmonary artery of a preterm baby. Catheter Cardio Int 2005;66:590–4.
[12] Song G. Control of biodegradation of biocompatible magnesium alloys. Corros Sci 2007;49:1696–701.
[13] Xu L, Zhang E, Yin D, Zeng S, Yang K. In vitro corrosion behaviour of Mg alloys in phosphate buffered solution for bone implant application. J Mater Sci Mater Med 2008;19:1017–25.
[14] Rettig R, Virtanen S. Composition of corrosion layers on magnesium rare-earth alloy in simulated body fluids. J Biomed Mater Res A 2009;88:359–69.
[15] Retting R, Virtanen S. Time-dependent electrochemical characterization of the corrosion of a magnesium rare-earth alloy in simulated body fluids. J Biomed Mater Res A 2008;85:167–75.
[16] Xu L, Yu G, Zhang E, Pan F, Yang K. In vivo corrosion behaviour of Mg–Mn–Zn alloy for bone implant application. J Biomed Mater Res A 2007;83:703–11.
[17] Gu X, Zheng Y, Cheng Y, Zhong S, Xi T. In vitro corrosion and biocompatibility of binary magnesium alloys. Biomaterials 2009;30:484–98.
[18] Zeng R, Dietzel W, Witte F, Hort N, Blawert C. Progress and challenge for magnesium alloys as biomaterials. Adv Eng Mat 2008;10:B3–B14.
[19] Li Z, Gu X, Lou S, Zheng Y. The development of binary Mg–Ca alloys for use as biodegradable materials within bone. Biomaterials 2008;29:1329–44.
[20] Inoue H, Sugahara K, Yamamoto A, Tsubakino H. Corrosion rate of magnesium and its alloys in buffered chloride solutions. Corros Sci 2002;44:603–10.
[21] Del Valle JA, Carreño F, Ruano OA. Influence of texture and grain size on work hardening and ductility in magnesium-based alloys processed by ECAP and Rolling. Acta Mater 2006;54:4247–59.
[22] Verdier S, van der Laak N, delalande S, Metson J, Dalard F. The surface reactivity of a magnesium–aluminium alloy in acidic fluoride solutions studied by electrochemical techniques and XPS. Appl Surf Sci 2004;235:513–24.

[23] Gulbrandsen E, Taftø J, Olsen A. The passive behaviour of Mg in alkaline fluoride solutions. Electrochemical and electron microscopical investigations. Corros Sci 1993;34:1423–40.
[24] El-Taib Heakal F, Fekry AM, Fatayerji MZ. Influence of halides on the dissolution and passivation behaviour of AZ91D magnesium alloy in aqueous solutions. Electrochim Acta 2009;54:1545–57.
[25] Li J-Z, Huang J-G, Tian Y-W, Liu C-S. Corrosion action and passivation mechanism of magnesium alloy in fluoride solution. Trans Nonferrous Met Soc China 2009;19:50–4.
[26] Yamamoto A, Terawaki T, Tsubakino H. Microstructures and corrosion properties on fluoride treated magnesium alloy. Mater Trans 2008;49:1042–7.
[27] Hassel T, Bach F-W, Krause C, Wilk P. Corrosion protection and repassivation after the deformation of magnesium alloys coated with a protective magnesium fluoride layer. Magnes Technol 2005:485–90.
[28] Cowan KG, Harrison JA. The dissolution of magnesium in Cl^- and F^- containing aqueous solutions. Electrochim Acta 1979;24:301–8.
[29] Lamolle SF, Monjo M, Rubert M, Haugen HJ, Lyngstadaas SP, Ellingsen JE. The effect of hydrofluoric acid treatment of titanium surface on nanostructural and chemical changes and the growth of MC3T3–E1 cells. Biomaterials 2009;30:736–42.
[30] Alonso C, García-Alonso C, Escudero M Patent. Electrolytic cell used for electrochemical analysis of metallic implant and cell culture interface. ES 2008;1595:1–10.
[31] Moulder JF, Stickle WF, Sobol PE, Bomben KD, editors. Handbook of X-ray photoelectron spectroscopy. Physical Electronics Division; 1992–1995.
[32] Wagner CD, Davis LE, Zeller MV, Taylor JA, Raymond RH, Gale LH. Empirical atomic sensitivity factors for quantitative-analysis by electron-spectroscopy for chemical-analysis. Surf Interface Anal 1981;3:211–25.
[33] Gutmanas EY. Materials with fine microstructures by advanced powder metallurgy. Prog Mater Sci 1990;34:261–366.
[34] Armstrong RW, Codd I, Douthwaite RM, Petch NJ. Plastic deformation in polycrystalline aggregates. Philos Mag 1962;7:45–58.
[35] Pérez P, Garcés G, Adeva P. Influence of texture on the mechanical properties of commercially pure magnesium prepared by powder metallurgy. Mater Sci 2007;42:3969–76.
[36] Gray JE, Luan B. Protective coatings on magnesium and its alloys—a critical review. J Alloy Compd 2002;336:88–113.
[37] Al-Abdullat Y, Tsutsumi S, Nakajima N, Ohta M, Kuwahara H, Ikeuchi K. Surface modification of magnesium by $NaHCO_3$ and corrosion behaviour in Hank's solution for new biomedical applications. Mater Trans 2001;48:1777–80.
[38] Baril G, Pébère N. The corrosion of pure magnesium in aerated and deaerated sodium sulphate solutions. Corros Sci 2001;43:471–84.
[39] Mueller W-D, Fernández Lorenzo de Mele M, Nascimento ML, Zeddies M. Degradation of magnesium and its alloys: dependence on the composition of the synthetic biological media. J Biomed Mater Res A 2009;90:487–95.
[40] Lamaka SV, Karavai OV, Bastos AC, Zheludkevich ML, Ferreira MGS. Monitoring local spatial distribution of Mg^{+2}, pH and ionic currents. Electrochem Commun 2008;10:259–62.
[41] Towler MR, Kenny S, Boyd D, Pembroke T, Buggy M, Hill RG. Zinc ion release from novel hard tissue biomaterials. Bio-Med Mater Eng 2004;14:565–72.